



UNIVERSITY OF LEEDS

This is a repository copy of *Electrochemical Response of Proprietary Microalloyed Steels to pH and Temperature Variations in Brine Containing 0.5% CO₂*.

White Rose Research Online URL for this paper:
<http://eprints.whiterose.ac.uk/153064/>

Version: Accepted Version

Article:

Onyeji, L and Kale, GM orcid.org/0000-0002-3021-5905 (2019) Electrochemical Response of Proprietary Microalloyed Steels to pH and Temperature Variations in Brine Containing 0.5% CO₂. *Corrosion*, 75 (9). pp. 1074-1086. ISSN 0010-9312

<https://doi.org/10.5006/2930>

© 2019 NACE International. This is an author produced version of a paper published in *Corrosion*. Uploaded in accordance with the publisher's self-archiving policy.

Reuse

Items deposited in White Rose Research Online are protected by copyright, with all rights reserved unless indicated otherwise. They may be downloaded and/or printed for private study, or other acts as permitted by national copyright laws. The publisher or other rights holders may allow further reproduction and re-use of the full text version. This is indicated by the licence information on the White Rose Research Online record for the item.

Takedown

If you consider content in White Rose Research Online to be in breach of UK law, please notify us by emailing eprints@whiterose.ac.uk including the URL of the record and the reason for the withdrawal request.



eprints@whiterose.ac.uk
<https://eprints.whiterose.ac.uk/>

Electrochemical Response of Proprietary Micro-Alloyed Steels to pH and Temperature Variations in Brine Containing 0.5% CO₂

Lawrence Onyeji, *Girish Kale.

School of Chemical and Process Engineering, University of Leeds, Leeds, LS2 9JT, United Kingdom.

ABSTRACT

The corrosion behavior of three new generation micro alloyed steels in CO₂ saturated brine at different pHs and temperatures was investigated using electrochemical (LPR, Tafel polarization and EIS) and surface analysis (SEM/EDS and XRD) techniques. The micro alloyed steels with ferrite-pearlite microstructures demonstrated better corrosion resistance than the specimen with bainitic structures. The analyses of the corroded surface revealed relative elemental changes of corrosion products revealing that the average ratio of Fe/O increased with increase in pH but decreased with increase in temperature. The electrochemical results indicated that the corrosion resistance of Steel C < Steel B < Steel A. The corrosion kinetics of the steels follow the empirical relation $y = Ax^B$ thus obeying the well-known Log-Log equation ($\log Y = \log A + B \log X$) which can be used to predict long time corrosion performance. The value of B represents the corrosion kinetics and it decreased with increase in pH depicting corrosion deceleration but increased with temperature signifying corrosion acceleration

Keywords: Corrosion, Brine, Microstructure, Micro-alloyed Steel, pH, Temperature.

*School of Chemical and Process Engineering, University of Leeds, Leeds, LS2 9JT, United Kingdom.

**Girish M. Kale

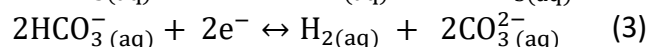
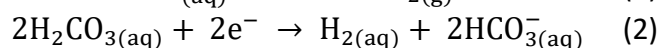
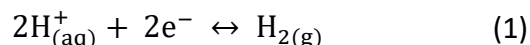
***G.M.Kale@leeds.ac.uk; (+44(0)1133432805) Corresponding Author.

INTRODUCTION

Dry CO₂ is by itself non-corrosive but in aqueous environment is highly corrosive leading to sweet (CO₂) corrosion which accounts for about 60% of equipment and facility failures with the attendant economic loss, ecological damages and loss of life and properties in oil and gas industry¹⁻⁴. This is why formation water, because of its high CO₂ content, is considered the most common impurity in oil and gas production². CO₂ dissolves in water to form aqueous solution consisting of carbonic acid (H₂CO₃) which is a weak but corrosive acid. Carbonic acid (H₂CO₃) dissociates in two steps to bicarbonate (HCO₃⁻) and carbonate (CO₃²⁻) ions respectively. Depending on temperature, pH and carbon dioxide partial pressure, these ions, through series of chemical and electrochemical reactions form protective iron carbonate (FeCO₃) in the presence of ferrous ion (Fe²⁺) when the product of Fe²⁺ and CO₃²⁻ exceeds the thermodynamic saturation limit beyond supersaturation conditions^{5,6}.

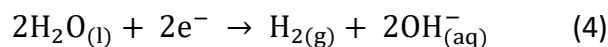
pH is one of the environmental factors that affects the rate and mechanism of CO₂ corrosion of steels through acidification of the medium^{6,7}. On one hand, decrease in pH increases corrosion rate of

steels while on the other hand, increase in pH decreases corrosion rate due to the formation of protective iron carbonate^{2,6-8}. When iron is immersed in CO₂-containing electrolyte, three major cathodic reactions involving the reduction of H⁺, HCO₃⁻ and H₂CO₃ may occur as shown in Equations 1 - 3.



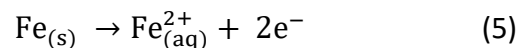
The contributions of each of these species (ions) in CO₂ corrosion of steel as reported by some authors^{2,5,7,9,10} depend on various parameters such as temperature, pH, and concentration.

Nazari, et al² and Moiseeva and Rashevskaya⁷ reported that the predominant cathodic reaction at pH < 4 is the reduction of hydrogen ion (Equation 1) and at 4 < pH < 6 the most important cathodic reaction is carbonic acid reduction (Equation 2) while at pH > 6 the reduction of bicarbonate ion dominates (Equation 3). Furthermore at pH ≥ 7, reduction of water as shown in Equation 4 dominates.



Dugstad⁵ and Tran, et al¹⁰ also reported similar cathodic reduction mechanism but noted that the reduction of carbonic acid may act as additional source of hydrogen (H⁺) ion leading to higher corrosion rate than hydrogen ion alone. Similarly, Linter and Burstein¹¹ and Remita et al¹² describe the situation whereby dissolved CO₂ enhanced the rate of hydrogen evolution reaction (HER) as buffering effect. In this case, dissolve CO₂ acts as a source of additional proton reservoir for HER which manifest in corrosion rate increase

The overall anodic dissolution of iron shown in Equation (5)



is strongly pH dependent and researchers^{5,9} have suggested various reaction steps. Nestic, et al⁹ argued that the anodic corrosion mechanism of iron as proposed by de-Waard and Williams¹³, up on which the work of Bockris, et al¹⁴ predicated, cannot be reliably applied to CO₂ corrosion. Therefore, they reported distinct and different anodic mechanisms at pH < 4 and pH > 5 with an intermediate region (4 < pH < 5) depicting a transition from one mechanism to another.

Temperature generally accelerates most chemical and electrochemical processes¹⁵⁻¹⁷. Increase in temperature decreases the solubility of CO₂ thus reducing its concentration in solution which in turn decreases corrosion rate. However, corrosion rate of steels generally increases at temperatures below 60°C. This is because, increase in reaction rate due to temperature increase dominates the decrease in corrosion rate caused by decrease in solubility. One could have therefore expected the corrosion of steels in CO₂ environments to depict a continuous increase with temperature. Nevertheless, experimental evidence¹⁸⁻²⁰ indicated that CO₂ corrosion of steels exhibits an intrinsic change in kinetics above 60°C. Zhao et al,¹⁸ observed that below 60°C, the corrosion product could not adhere on the steel surface resulting in severe corrosion whereas at 80°C, they observed the presence of FeCO₃ which could not provide effective corrosion protection due to poor surface adhesion. However, between 80°C and 140°C, a compact and adherent corrosion

product consisting of mainly FeCO₃ was observed which drastically reduced the corrosion rate. Above 140°C, some other researchers^{6, 20, 21} reported the presence of complex corrosion products consisting of Fe₃O₄ and FeCO₃ which further increased the corrosion resistance. Contrary to this, Al-Hassan, et al¹⁹ reported that FeCO₃ formed within the activation control region was non-protective. However, at temperatures 58°C and 65°C the authors observed the formation of more stable iron hydroxycarbonate (Fe(OH)₂CO₃) which was believed to be responsible to the reduction in corrosion rate.

The effect of all other environmental factors affecting CO₂ corrosion of micro-alloyed steels are directly or indirectly influenced by the intrinsic change in CO₂ corrosion mechanism with respect to temperature variation¹⁵. More recently, Schmitt and Horstemeier⁶ reported that temperature has effect on the morphology and crystallinity of the protective carbonate scales. At temperatures above 90°C, the scale composed of well-defined, well packed and adherent crystals of FeCO₃ providing adequate protection but at lower temperatures porous, loose and flat grain-products with little or no protection were formed.

Micro-alloyed steels have excellent combination of mechanical properties such as strength, toughness, formability and weldability. Hence they have found wide acceptance as preferred material for oil and gas pipelines. These excellent properties of micro-alloyed steels have been attributed to the grain refining ability of micro addition of alloying elements, controlled rolling, application of appropriate processing technologies and heat treatments with the attendant microstructures²². Microstructures of steel significantly depend on the chemicals composition and thermo-mechanical treatment used for its production. It has been reported^{19, 23} that microstructures play important role on the corrosion resistance of micro-alloyed steels since different phases provide sites for anodic and cathodic reactions. This was evidenced in our previous work²⁴ which showed that the micro-alloyed steels with fine grain structures and less ferrite/pearlite ratio exhibited more susceptibility to corrosion attack. This report, in agreement with other researchers²⁵⁻²⁷, also showed that high carbon content in steel can suppress the corrosion resistance effect of chromium (Cr) when the Cr content is less than 1%. In this current work, the corrosion characteristics of these micro-alloyed steels were further investigated at various pH values and temperatures in 3.5 wt% NaCl solution saturated with 0.5% CO₂.

2.0 Experimental Procedures

2.1 Materials and Specimen Preparation

Three micro-alloyed steels designated as Steel A, Steel B and Steel C with chemical composition shown in Table 1 were used in this study. Steels A and B were supplied as quenched and tempered with ferrite/pearlite microstructure while Steel C has ferrite/bainite structures. These microstructures are attributed to the chemical composition of the steel and the thermo-mechanical treatment deployed during production. Depending on the profile of the as-supplied steel samples, a cylindrical shape of 4.91 cm² surface area was machined from Steel A while Steels B and C have a rectangular surface area of 2.88 cm². Copper wires were soldered to each of the specimens and enclosed in non-conductive epoxy resin leaving only one uncovered surface as the working electrode. The working surface was wet polished using silicon carbide paper up to P1200 grit fineness. The polished surface was rinsed with distilled water, degreased with methanol, dried in warm air and immediately immersed in the electrochemical cell for corrosion experiment.

2.2 Electrochemical Solution (Electrolyte)

The electrolyte containing 3.5 wt% NaCl was prepared from analytical grade reagent in 1 litre glass cell. The experiments were performed at

three pH values (3.5, 5.0 and 6.5) and three temperatures (25°C, 45°C and 60°C) respectively. Before the start of each electrochemical test, the electrolyte was bubbled with 0.5% CO₂ gas in N₂ for 3 hours to simultaneously deoxygenate and saturate the solution. According to literature report,⁵ only very small fraction (0.2% to 1%) of dissolved CO₂ hydrates to form carbonic acid which is the precursor for CO₂ corrosion attack. Therefore, the use of 0.5% CO₂ in N₂ was to investigate the effect of lower concentration of CO₂ gas during CO₂ corrosion. The pH of the solution was adjusted using sodium bicarbonate (NaHCO₃) or Hydrochloric acid (HCl) while the desired temperature was maintained using a hotplate with a feedback control thermocouple immersed in the solution. With the help of a magnetic stirrer, the hotplate was also used to gently stir the electrolyte at 200 rpm in order to maintain homogeneous temperature and concentration within the bulk electrolyte.

2.3 Electrochemical tests

The corrosion characteristics of the micro-alloyed steels were assessed using linear polarization resistance (LPR), Tafel polarization and electrochemical impedance spectroscopy (EIS) techniques in 3.5 wt% NaCl solution saturated with 0.5% CO₂ in N₂ at different pH and temperatures respectively. Tafel parameters were obtained using Tafel extrapolation techniques as outlined in^{28, 29}. The values of polarization resistance (R_p) and corrosion resistance were calculated using the *i*_{Corr} extracted from Tafel extrapolation in Equations 6 and 7.

$$R_p = \frac{\beta_A * \beta_C}{2.303(\beta_A + \beta_C)} * \frac{1}{i_{Corr}} \quad (6)$$

$$C_R \text{ (mm/Y)} = \frac{3.27 * 10^{-3} * i_{Corr} * (E.W)}{\rho} \quad (7)$$

Where: β_A and β_C = Tafel constants (mV/decade), E.W = equivalent weight (g), ρ = Density (g/cm³). Solartron SI 1287 equipped with CorrWare for data acquisition and CorrView for data display and interpretation was used. For EIS experiments, Solartron SI 1260 impedance/gain-phase analyser equipped with ZPlot was used for data collection while the experimental results were interpreted based on an equivalent electrical circuit (EEC) using a suitable fitting procedure of ZView.

Corrosion potential was initially monitored for 13 minutes in open circuit condition allowing it to reach a stable value. This was alternated with linear polarization resistance (LPR) measurement for 24 hours at a scan rate of 0.25 mV/sec and scan range of ± 15 mV_(Ag/AgCl). Tafel polarization curves were obtained within a sweep range of ± 250 mV_(Ag/AgCl) and scan rate of 0.5 mV/sec. All the electrochemical data were obtained using Stern-Geary constant of 26. This was to ensure uniformity of the assessment parameters since different materials are being compared. A two-electrode electrochemical cell, in which the steel specimen was the working electrode and platinum coil the counter electrode was used for electrochemical impedance spectroscopy (EIS). EIS measurement was conducted at OCP with potential perturbation of 5 mV RMS. This potential perturbation gave the best and un-scattered impedance spectra than the higher potentials. Data were acquired using a frequency range of 100 KHz to 0.1 Hz. The specimen, at the end of each experiment, was immediately rinsed with distilled water to remove soluble salts on the surface, dried with nitrogen gas and stored in a desiccator until surface analysis was conducted. All the electrochemical tests were repeated 2 to 3 times to ensure reproducibility.

2.4 Surface Analysis

The morphologies and the chemical composition of the corrosion products formed on the surface of the specimens were characterized using Carl Zeiss EVO MA15 scanning electron microscope equipped with Oxford Instruments Aztec Energy EDS system while the phase composition of the corrosion products were determined using XRD Bruker D8 Detector X-ray diffractometer.

3.0 Results

3.1 As-received microstructure

The samples were received as quenched and tempered as revealed by the SEM secondary electron micrographs of the specimens shown in Figure 1. This figure shows that Steels A and B consist of light and dark zones which are colonies of pearlite within the ferrite matrix. The insets are the backscattering images of the samples. The lamellae structures of the pearlite phase are clearly visible in the micrographs of Steel A. Another distinctive feature of the micrographs of these specimens is their grain (phase) size which within each steel are the same and uniformly distributed. However, the grain sizes amongst the steels differ from each other displaying a ranking order of $A_{GS} > B_{GS} > C_{GS}$ as shown in Table 2. This table revealed the average grain size, ASTM Grain Size number and the Ferrite/Pearlite Ratio (%) of the samples. The SEM micrographs of Steel C shown in Figures 1(c) revealed bainitic structure with evenly distributed acicular ferrites³⁰.

3.2 Tafel Polarization

The Tafel plots of Steel A as a function of pH (at 60°C) and temperature are shown in Figure 2 (A) and Figure 2 (B) respectively. The Tafel curves of Steels B and C exhibited similar characteristics at various pH and temperatures. The Tafel parameters obtained using Tafel extrapolation techniques are shown in Tables 3 and 4 for pH and temperature variations respectively.

It can be observed from Figure 2 that the plots of potential (vs OCP) versus current density are similar for all the steel specimens in both pH and temperature conditions suggesting that the corrosion mechanism is the same^{31,32}. The anodic current densities increased with increase in potential particularly within the low overvoltage depicting a well-defined Tafel slopes. This signified an active dissolution of the specimens and revealed that no corrosion product was formed. However at about -600 mV_{Ag/AgCl} (Sat. KCl), the kinetics of current densities reduced with increase in potential suggesting the occurrence of pseudo-passivation with the appearance of seemingly current plateaus. These signatures became more pronounced as pH decreases than with increasing temperature. This behavior was also reported by Ochoa, et al³³ and Henriquez et al¹⁶ who attributed it to the accumulation of corrosion product that partially block the surface of the steel with increase in immersion time. The witnessed anodic current plateau also indicated the formation of poorly protective anodic corrosion film¹⁵. The cathodic Tafel curves in both conditions demonstrated a well-defined Tafel slopes.

3.3 Linear Polarization Resistance (LPR)

The LPR curves for the specimens in 3.5 wt% NaCl solution saturated with 0.5% CO₂ at 60°C and different pH values are presented in Figure 3. Figure 3 shows that the corrosion rate decreased very rapidly within the first 3 hours at pH 5 and 6.5 whereas at pH 3.5 the corrosion rate decreased much more slowly before attaining a stable value for all specimens used in this study. For instance, Steel B attained a stable value at about 0.4 mm/y in pH 3.5 but the stable corrosion rate decreased to 0.3 mm/y in pH 5.0 and decreased further to about 0.1 mm/y in pH 6.5. Steels A and C showed similar trend. Also the period during which the corrosion rate became relatively stable decreased with

increase in pH signifying that the rate of deposition of corrosion products increased with increase in pH. Another notable feature of Figure 3 is the corrosion rate (CR) of the steels which showed that Steel A < Steel B < Steel C at all the three pH values.

Figure 4 shows the average corrosion rate (CR) of the Steels in unbuffered 3.5 wt% NaCl solutions saturated with 0.5% CO₂ after 24 hours and at different temperatures. From this figure, it can be observed that the specimens demonstrated similar (but not with the same magnitude) initial decrease in corrosion rate as shown in Figure 4 before stabilizing. Figure 4 indicates that the stable value of the corrosion rate of the specimens increased with temperature. For instance the stable corrosion rate of Steel A increased from 0.1 mm/y at 25°C to 0.2 mm/y at 45°C and further increased to 0.3 mm/y at 60°C. The corrosion resistance of the steels as a function of temperature exhibited similar ranking order as in pH variations. The error bars shown in Figures 3 and 4 represent minimum and maximum values obtained from repeated experiments.

Figure 5 shows the log-log plots of weight loss (W) against time (t) for the 24 hours LPR data of Steel A corroded in 3.5 wt% NaCl solutions saturated with 0.5% CO₂ at different pH (Figure 5A) and temperatures (Figure 5B). The LPR data were converted to weight loss using Equation 8.

$$CR = \frac{\Delta W * K}{\rho * A * t} \quad (8)$$

Where

K = Constant = 8.76 x 10⁴, ρ = Alloy density (g/cm²), A = Exposed surface area (cm²) and t = Exposure time (hr)

Figure 5 shows the linear regression curves and the long-time prediction models given by the function expressed in Equation 9 which can be represented by the well-known log-log relationship of Equations 10.

$$W = At^B \quad (9)$$

$$\text{Log } W = \text{Log } A + B \text{Log } t \quad (10)$$

Where W is weight loss (mg), t is time (hrs) while A is constant representing the intercept on the weight loss axis. B is also a constant depicting the slope of the plot. The values of these constants and the correlation coefficient (R²) are shown in Figure 5.

The values of B in the long-time prediction models shown in Figure 5, signify the corrosion kinetic of the corroding steels. B in general depends on the type of metal or alloy, on the medium in which the material is exposed and on the exposure conditions. B < 1 indicates corrosion deceleration process, B > 1 means an acceleration process while B = 1 suggests that the process is in equilibrium or steady state³⁴⁻³⁶. The value of B for all the specimens decreased with increase in pH depicting corrosion retardation with increasing pH but increased with temperature signifying increase in corrosion kinetic with temperature. This corroborates with the LPR results of this work shown in Figures 3 and 4. R² values are almost equal to 1 for all the specimens in both pH and temperature variations indicating that the fitted model satisfied all the variables of the response data³⁵.

3.4 Electrochemical Impedance Spectroscopy (EIS)

Figure 6 shows the EIS spectra of steel A corroded in 0.5% CO₂ saturated 3.5 wt% NaCl at different temperatures (Figures 6a and 6b) and different pH (Figures 6c and 6d) after 24 hours linear polarization resistance experiments. This figure reveals that the Nyquist plots for

steel A at different temperatures (Figure. 6a) and pH (Figure. 6c) displayed similar features of one semi-capacitive loops at high frequency. According to literature^{37,38}, this can be ascribed to the non-homogeneity of the surface of the specimens, frequency dispersion and mass transport resistant. This figure also shows that the radius of the capacitive loop of steel A decreased with increase in temperature (Figure. 6a) but increased with increase in pH (Figure. 6c). The same trend of behaviour was also observed with steels B and C.

The Bode plots for the micro-alloy steel A are shown in Figure. 6(b) for different temperature and Figure. 6(d) for different pH. This figure shows that the high frequency impedance magnitude ($|Z|$), which represents the solution resistance (R_s), is about 25 $\Omega \cdot \text{cm}^2$ and 5 $\Omega \cdot \text{cm}^2$ for steel A at temperature and pH conditions respectively. At low frequency is the impedance magnitude ($|Z|$), which signifies the charge transfer resistance (R_{ct}). On the other hand the phase angle value of steel A at high frequency in both conditions is 0° . This suggests that the impedance value at high frequency is solely dependent on the resistance of the electrolyte. The maximum phase angle values for both conditions appeared within the intermediate frequencies demonstrating a highest phase angle of 55° at 25°C and 65° at pH 6.5 for Steel A. At low frequency, the phase angle values of steel A lie between $15^\circ - 30^\circ$ and $15^\circ - 20^\circ$ for temperature and pH variations respectively. The other two steels used in this work exhibited the same behavioral trend. This is in agreement with the report of Luo, et al³⁷ and chen Bian, et al³⁹.

To quantify the effects of temperature and pH on the EIS results of the specimens corroded in 3.5 wt% NaCl solution saturated with CO_2 , the simple Randle cell (equivalent electrical circuit, EEC) model shown in Figure. 7 was adopted. This model consists of three main elements which include the electrolyte resistance (R_s), the double layer capacitance (C_{dl}) and the charge transfer resistance (R_{ct}). The electrolyte resistance (R_s) depicts the resistance of the solution between the working and reference electrodes. On the other hand, the double layer capacitance (C_{dl}) and the charge transfer resistance (R_{ct}) which are in parallel represent the corrosion reactions at the metal/electrolyte interface. To reduce the effect of surface irregularities and compositional inhomogeneity of the steels, the constant phase element (CPE) was introduced in the equivalent electrical circuit (EEC) in place of pure double layer capacitance^{16,39}. CPE has been defined as in Equation 9.

$$Z_{\text{CPE}} = \frac{1}{Y_0} (j\omega)^{-n} \quad (11)$$

Where Y_0 is the magnitude of CPE, $\omega = 2\pi f$ is the angular frequency (radians/second), f is the ordinary frequency (Hertz), j is the imaginary number and n is the dispersion coefficient related to surface non-homogeneity. Depending on the value of n , CPE may be pure resistor (ie if $n = 0$ then $Z_0 = R$), pure capacitor (meaning that $n = 1$ when $Z_0 = C$) or inductor (ie when $n = 0.5$ and $Z_0 = W$)^{3,16,39}.

Figure. 8 shows a representative of the fitted results of the impedance spectra for steel A corroded in 3.5 wt% NaCl saturated with 0.5% CO_2 at 60°C (Figures. 8a and 8b) and at pH 3.5 (Figs. 8c and 8d). It can be observed from this figure that the measured results matched relatively very well with the fitted results in both Nyquist and Bode plots. This is made more vivid by the moderately low % error of the fitted electrochemical parameters listed in Tables 5 and 6 for temperature and pH variations respectively. Table 5 shows that as temperature increased, the charge transfer resistance (R_{ct}) decreased while the double layer capacitance (CPE_{dl}) increased. Alternatively, Table 6 reveals that the charge transfer resistance (R_{ct}) increased while the double layer capacitance (CPE_{dl}) decreased with increase in pH. The low frequency impedance magnitude ($|Z|$), which corresponds to the charge transfer resistance (R_{ct}) obtained from EIS fitted data, lie between 5000 – 14,000

$\Omega \cdot \text{cm}^2$ and 5000 – 56,000 $\Omega \cdot \text{cm}^2$ for temperature and pH variations respectively as recorded in Tables 5 and 6. Decrease in charge transfer resistance (R_{ct}) indicates faster rate of reactions at the corrosion product/electrolyte interface. This corroborates the results of the LPR and Tafel polarization as presented in Sections 3.2 and 3.3 reiterating that the corrosion rate of the steels increased with increase in temperature but decreased with increase in pH. Similar results have been reported⁴⁰.

To estimate the average value of the double layer capacitance (C_{dl}) associated with the parameters CPE and n in Table 5 and 6, Burg's formula shown in Equation 12 was used. This formula corrects (C_{dl}) to its real value when CPE and R_{ct} are in parallel but in series with R_s (Figure 7)⁴¹⁻⁴³

$$C_{dl} = \text{CPE}_{dl}^{\frac{1}{n}} \left(\frac{1}{R_s} + \frac{1}{R_{ct}} \right)^{\frac{(n-1)}{n}} \quad (12)$$

The values of (C_{dl}) obtained using Equation 12 are inserted in Tables 5 and 6 for temperature and pH variations respectively. Table 5 showed that the double layer capacitance (C_{dl}) increased with increase in temperatures. This is an indication of the increasing rate of corrosion with increase in temperature which can be attributed to the non-formation of corrosion products at temperatures less than 60°C . This is in agreement with the of Marta, et al⁴⁴. On the other hand, Table 6 revealed a decrease in C_{dl} with increase in pH for the steels indicating the formation of corrosion product with increase in pH. This is consistent with the results of LPR, Tafel polarization and surface analyses.

3.5 Surface Analysis

The SEM micrographs of the surface of the corroded steel A at pH 3.5 and 60°C are shown in Figure 9. This figure revealed that no corrosion product was formed on the surface of steel but showed some embossed patterns. These embossed patterns became more pronounced with decrease in pH and increase in temperature. The same features were observed in the SEM micrograph of steel B. The embossed (protrusions) patterns are the non-dissolved lamellar cementite which were left behind after the ferrites phase has been preferentially dissolved.

In comparison to steels A and B, steel C with bainitic structure displayed a flaky, cracked and loosely held corrosion product with some partially peeled corrosion product layers of the specimen corroded in pH 3.5 as shown in Figure 10 (a). On the other hand, the SEM micrograph of steel C corroded at temperature 60°C showed cracked (indicated with arrows in Figure 10 (b)) corrosion product on the surface which permitted the ingress of active corrosion species to the steel substrate and thus continued the corrosion process. This led to the witnessed high corrosion rate of steel C as shown in Table 4. Tables 7 and 8 show the representative EDS Elemental analysis of steels A and C at two locations on the SEM Micrographs shown in Figures 9 and 10 respectively. Figure 11 shows the XRD pattern of steel A corroded in 3.5 wt% NaCl solution saturated with CO_2 at 60°C and different pH. The XRD pattern showed Fe_3C and Fe_3O_4 as the main phases on all the three steel substrates.

4.0 Discussion:

The microstructures of as received micro-alloy steels used in this work as shown in Figure 1 consist of ferrite-pearlite and ferrite-bainite phases with different grain sizes which can be ascribed to the effects of chemical composition and thermo-mechanical treatment involved in their production^{19,33,45,46}. Microstructures significantly affect the corrosion behavior of micro-alloy steels^{19,47} because the shape, size and distribution of the phases greatly influence corrosion rate^{5,19}. Steels A and B consist of ferrite-pearlite structures with steel A having more ferrite phase (dark region) and larger grain size than Steel B as revealed by Fiji-ImageJ analysis and ASTM grain size number computed according to ASTM E112-12 standard and shown in Table 2⁴⁸. On the other hand, the bainitic structure of Steel C as shown in Figure 1 (C) are believed to

have formed when the decomposition of austenite to ferrite and pearlites is restrained by the presence of micro-alloying elements^{30, 49-51}. Kermani and Morshed²⁰ and Kermani et al²⁵ identified Cr and Mo as alloying elements that retard decomposition of martensite or austenite to ferrites and carbides. Steel C as shown in Table 1 contains more Cr (0.99 wt%) and Mo (0.46 wt%) than the other steels. This could have been the reason for bainitic microstructure.

When a freshly polished micro-alloy steel with ferrite-pearlite microstructures is immersed in brine, selective dissolution of the ferrite phase takes place leaving the cementite (Fe_3C) on the metal surface which is more difficult to dissolve. Fe_3C being an electronic conductor enhanced the corrosion rate by causing galvanic effect and acting as cathodic site for the hydrogen evolution reaction (HER). The adherence and protective properties of corrosion product films are related to the presence of these cementite (Fe_3C) platelets which strengthen and anchor the films to the specimen substrate^{38, 50}. Fe_3C is not a corrosion product but merely existed in the scale as a result of its presence in the steel and acts as cathode while the ferrite acts as the anode in ferrite-pearlite microstructure^{19, 21, 38, 52}. Also the preferential dissolution of ferrite resulted in high ferrous ion (Fe^{2+}) concentration between the lamellar Fe_3C which became the site for cathodic reactions³³ resulting to Steel B with higher cathode-anode (pearlite-ferrite) ratio being more susceptible to corrosion attack than Steel A. Pearlite phase has also been observed to increase with carbon content. Thus, Steel B with higher carbon content (Table 1) has more pearlite phase and consequently greater cathode to anode ratio thereby resulting in higher corrosion rate than Steel A as shown in Figures 2 and 3. Similar results have been reported^{1, 53-56}.

The pH of the solution play important role in determining the rate and mechanism of CO_2 corrosion of carbon steels. It has been observed that the dominant cathodic reaction in CO_2 corrosion of steels is dependent on the pH of the solution³. pH affects corrosion rate of micro-alloy steels through acidification of the medium whereby the corrosion rate increased with decrease in pH. This phenomenon is demonstrated by the results of the electrochemical corrosion tests conducted in this work as shown in Figure 3. The highest corrosion rate was recorded at low pH (3.5) which can be ascribe to the cathodic reduction of H^+ ions with the corresponding anodic dissolution of the substrate through the process of hydrogen evolution reaction as expressed in Equation (1). At pH 5, Nazari et al² reported the reduction of carbonic acid (H_2CO_3) shown in Equation (2) as the dominant cathodic reduction. Tran et al¹⁰ and Linter and Burstein¹¹ described the mechanism in which adsorbed carbonic acid directly reduced on the surface of the steel as buffering effect. In such situation, carbonic acid acts as an addition source of H^+ ion to the corrosion process. This dual source of H^+ ions explained why there was higher corrosion rate at pH 5 than at pH 6.5 where the only cathodic reaction was due to hydrogen H^+ ions provided by the dissociation of bicarbonate ions (HCO_3^-)^{2, 7, 10}. In other words, the reduction of additional H^+ ions is not favored at pH 6.5 thus resulting in low corrosion rate¹⁰. This is in agreement with the results of the LPR corrosion rate shown in Figures 3, the Tafel extrapolation parameters recoded in Table 3 and EIS fitted parameters listed in Table 6.

Temperature is one of the primary environmental factor of CO_2 corrosion. Temperature generally accelerates most chemical and electrochemical processes by affecting gas solubility, reaction kinetics and equilibrium constant¹⁵⁻¹⁷. Generally, corrosion rate of steels in CO_2 environments increases with increase in temperature up to 60°C but exhibits an intrinsic change at 60°C due to increase in kinetic of precipitation of FeCO_3 on the surface of the steels. This formed a diffusion barrier for the active corrosion species²¹ to reach the steel surface. There is no general agreement on the threshold temperature that will precipitate enough FeCO_3 to prevent the corrosion species from

reaching the steel substrate. This could be linked to the myriad of factors such as pH, immersion time, corrosion potential and flow condition influencing CO_2 corrosion of steels¹⁶. Thus different authors have reported different threshold temperature ranging from 60°C to 100°C depending on other environmental factors^{18, 49, 53}. Al-Hassan et al¹⁹ argued that un-protective FeCO_3 can form at temperatures below 60°C but adduced that $\text{Fe}(\text{OH})_2\text{CO}_3$ is responsible for the reduction in corrosion rate of alloyed steels at temperatures above 65°C. The three electrochemical corrosion techniques deployed showed that within the experimental conductions of this work, the corrosion rate of the three specimens increased with increase in temperature and concurring that the corrosion resistance of steel A > steel B > steel C.

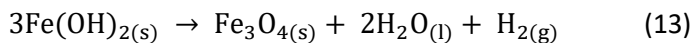
It can be observed from Tables 3 and 4 showing the R_p and Tables 5 and 6 showing the R_{ct} , that R_{ct} for the specimens is greater than the corresponding R_p . This was because, the R_{ct} values determined from fitting the EIS data was influenced by the irreversible adsorption-desorption process of an adsorbed intermediate products occasioned by 24 hours LPR. These intermediate products formed physical barrier for the active electrochemical species not accessing the surface of the specimen. This slowed down the kinetic process involved in corrosion resulting in higher corrosion resistance (R_{ct})⁶. This was revealed by the lower values of R_p obtained from LPR which was conducted under charge transfer controlled corrosion process than the R_{ct} from EIS. Therefore, it can be adjudged that R_{ct} from EIS underestimated the corrosion rate of the specimens.

The EDS analyses of all the specimens investigated at different pH (3.5, 5 and 6.5) and at different temperatures (25°C, 45°C and 60°C) as shown in Tables 7 and 8 respectively revealed that the main elements of the corrosion products were Fe, C and O with traces of Mn, Cr, Cu and Si. These elements were uniformly distributed within the corrosion product. This uniform distribution of the corrosion product and the large grain size could have contributed to the lower corrosion rate exhibited by steel A in both pH and temperature conditions. As observed from the microstructures of the specimens (Figure 1) and verified by Fiji-ImageJ analysis (Table 2), steel A has large grain size and ultimately fewer grain boundaries than steel B which on the other hand has fine grain structure with higher volume fraction of grain boundaries and triple junctions. The grain size-corrosion resistance relationship has been a topic of debate in literature. Some authors^{38, 57, 58} have reported that in ferrite-pearlite microstructures, pearlites precipitate and residual stresses cum alloying elements segregate along the grain boundaries resulting to high energy density at the grain boundaries. All these culminate to higher energies at the grain boundaries with the attendant high chemical activities. In this case, grain size reduction increases the susceptibility of steel to corrosion attack because high volume fraction of grain boundaries act as cathodic sites on electrochemical process. In contrast, others authors^{59, 60} observed that decrease in grain size decreases the susceptibility of ferrous alloys to corrosion attributing this effect to improved passive film stability, which could be the result of increased rates of diffusion in fine-grained structures. Yet another group of researchers^{57, 61-63} argued that the effect of grain size on the corrosion of steels could be detrimental or beneficial depending on certain processing variables and environment conditions such as pH, electrolyte, residual stresses, processing routes, etc. According to Zeiger, et al⁶¹ fine grain size is detrimental to corrosion resistance in electrolytes that simulate active behavior but beneficial in electrolytes that promote passivity. In the present work, steel A with fewer grain boundaries has less cathodic sites and ultimately demonstrated lower susceptible to corrosion attack than steel B.

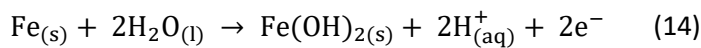
The average ratio of Fe/O (wt%) computed from EDS analysis of at least three points (two points shown in Figures 9 and 10) on the surface of the corroded specimens increased with increase in pH but decreased

with increasing temperature. For instance, the average ratio of Fe/O for Steel A is 20.46, 24.81 and 30.55 for pH 3.5, pH 5 and pH 6.5 respectively. For the temperature variation, the same ratio for Steel A are 61.78, 49.30 and 41.17 at 25°C, 45°C and 60°C respectively. This resulted in changes on the surface morphology of specimen due to the increased dissolution of Fe as pH decreased and as temperature increased. This is in agreement with the report of Yin et al⁵⁴ and corroborated the LPR results of this work. Since Fe, C and O are the main elements of the corrosion product, it may be assumed, as is the inherent attribute of CO₂ corrosion of steel, that the corrosion product was FeCO₃. However, FeCO₃ was not detected by the XRD analyses of the corroded specimens in both conditions, as shown for Steel A in Figure 11 for pH variation.

The XRD spectra showed Fe₃C as the main phase on the surface of all the steel substrates. Fe₃C is part of the steel microstructure left behind after the anodic dissolution of Ferrite⁵⁵. It means that the concentrations of the dissolved Fe²⁺ ions and the CO₃²⁻ ions from carbonic acid were not high enough to precipitate FeCO₃^{55, 56}. The traces of Fe₃O₄ in the XRD patterns can apparently be attributed to the preceding decomposition of Fe(OH)₂ as shown in Equation (13). The seemingly higher Fe₃O₄ peak at pH 3.5 as shown in Figure 11 is because Fe₃O₄ is thermodynamically more stable than Fe(OH)₂ at low pH which may be attributed to hydrogen evolution of Equation 13



Fe(OH)₂ on the other hand is the product of the overall anodic electrochemical reaction for ferrous metals as expressed in Equation 14⁷ according to the pH dependent reaction mechanism proposed by Bockris¹⁴



The SEM micrographs of the corroded surface of Steel C at pH 3.5 and 60°C for both conditions respectively are shown in Figure 10 (a and b). This figure revealed a sludge like corrosion products which allowed the ingress of corrosion species to the steel substrates leading to severe corrosion spallation. Similar characteristics was observed by Wu, et al⁶⁴. Steel C also has relatively higher Cr and Mo content than steels A and B. These elements improve corrosion resistance by favoring passivity^{19, 20, 25, 26, 30}. However, this influence was not observed in the present work. Kermani, et al²⁵ and Kermani and Morshed²⁰ reported that an optimum Cr content, subject to other alloying constituents and heat treatment, had a significant beneficial role on the CO₂ corrosion of the steels. Ueda, et al²⁶ observed that below 60°C, the effect of Cr addition in enhancing corrosion resistance is effective with Cr content more than 1 wt%. It has also been reported^{21, 65} that the corrosion resistance of steels decreased with increased carbon content. This means that due to high carbon content and Cr content < 1 wt%, the effect of Cr in enhancing corrosion performance of steel C was not pronounced. This is because of the high carbon content which formed carbides with Cr²⁵⁻²⁷ leading to increased cathodic site and therefore increased corrosion rate^{19, 30}

Conclusion

The corrosion behavior of three new generation of micro-alloyed steels with varying chemical compositions and microstructures and whose corrosion characteristics have not been properly understood were investigated using electrochemical techniques in brine saturated with 0.5% CO₂ at different pH and temperatures. The surface of the corroded steels were characterized using SEM/EDS and XRD analyses. The results of the experiments showed that the three micro-alloyed steels demonstrated mild variations in corrosion rate which can be attributed to chemical composition and microstructures. Steels A and B with ferrite-pearlite microstructures, large grain size and less carbon content

exhibited better corrosion resistance in both pH and temperature conditions than steel C. The EDS analysis of the corroded surfaces of the steels showed relative changes of the surface morphology of the steels which was revealed by the increase in the average ratio of Fe/O with increased in pH but decreased with increase in temperature. This signified an increase in iron dissolution with pH decrease and temperature increase. The corrosion kinetics of the steels obeyed the well-known log-log equation ($\text{Log } W = \text{Log } A + B \text{Log } t$) and the values of B for all the specimens increased with temperature signifying corrosion acceleration but decreased with increase in pH depicting corrosion retardation. The corrosion rate of all the specimens increased with increase in temperature but decrease with increase in pH within the experimental conditions. This is evidenced by the average corrosion current density which decreased from 6.7 μA/cm² at pH 3.5 to 5.3 μA/cm² at pH 5 and 5.1 μA/cm² at pH 6.5 for Steel A. On the other hand, the average corrosion current density increased from 2.4 μA/cm² at 25°C to 5.0 μA/cm² at 45°C and to 7.1 μA/cm² at 60°C for Steel A. In general the results of the various electrochemical corrosion and the surface analyses techniques employed corroborated each other and showed that the corrosion resistance of the specimens can be ranked as Steel C < Steel B < Steel A.

Acknowledgement

We wish to acknowledge and appreciate the sponsorship of this work by Petroleum Technology Development Fund (PTDF), Abuja, Nigeria. The authors wish to thank Professor B. Kermani for liaison with the steel industry that supplied the micro-alloyed steel samples used in this investigation.

Reference

1. L. T. Popoola, A. S. Grema, G. K. Latinwo, B. Gutti and A. S. Balogun, International Journal of Industrial Chemistry **4** (1), 1-15 (2013).
2. M. H. Nazari, S. Allahkaram and M. Kermani, Materials & Design **31** (7), 3559-3563 (2010).
3. J. Sun, G. Zhang, W. Liu and M. Lu, Corrosion Science **57**, 131-138 (2012).
4. Y. Zhang, X. Pang, S. Qu, X. Li and K. Gao, Corrosion Science **59**, 186-197 (2012).
5. A. Dugstad, "Fundamental Aspects of CO₂ Metal Loss Corrosion Part I: Mechanism", CORROSION 2006, paper no. 06111, (Houston, TX, 2006), p. 1-18.
6. G. Schmitt and M. Horstemeier, "Fundamental Aspects of CO₂ Metal Loss Corrosion – Part II: Influence of Different Parameters on CO₂ Corrosion Mechanisms", CORROSION 2006, paper no. 06112, (Houston, TX, 2006), p. 1-26
7. L. Moiseeva and N. Rashevskaya, Russian journal of applied chemistry **75** (10), 1625-1633 (2002).
8. Y. Prawoto, K. Ibrahim and W. Wan Nik, Arabian Journal for Science and Engineering **34** (2), 115 (2009).
9. S. Nescic, N. Thevenot, J. L. Crolet and D. Drazic, "Electrochemical Properties of Iron Dissolution in the Presence of CO₂ - Basics Revisited", CORROSION 1996, paper no. 03, (Houston, TX, 2006), p. 3/1
10. T. Tran, B. Brown and S. Nescic, "Corrosion of Mild Steel in an Aqueous CO₂ Environment – Basic Electrochemical Mechanisms Revisited", CORROSION 2015, paper no. 5671, (Houston, TX, 2015).
11. B. Linter and G. Burstein, Corrosion science **41** (1), 117-139 (1999).
12. E. Remita, B. Tribollet, E. Sutter, V. Vivier, F. Ropital and J. Kittel, Corrosion Science **50** (5), 1433-1440 (2008).
13. C. De Waard and D. Milliams, Corrosion **31** (5), 177-181 (1975).

14. J. M. Bockris, D. Drazic and A. Despic, *Electrochimica Acta* **4** (2), 325-361 (1961).
15. M. Gao, X. Pang and K. Gao, *Corrosion Science* **53** (2), 557-568 (2011).
16. M. Henriquez, N. Pébère, N. Ochoa and A. Vilorio, *Corrosion* **69** (12), 1171-1179 (2013).
17. G. Lin, M. Zheng, Z. Bai and X. Zhao, *Corrosion* **62** (6), 501-507 (2006).
18. J. Zhao, Y. Lu and H. Liu, *Corrosion Engineering, Science and Technology* **43** (4), 313-319 (2008).
19. S. Al-Hassan, B. Mishra, D. Olson and M. Salama, *Corrosion* **54** (6), 480-491 (1998).
20. M. Kermani and A. Morshed, *Corrosion* **59** (8), 659-683 (2003).
21. T. Tanupabrungrun, B. Brown and S. Nestic, "Effect of pH on CO₂ Corrosion of Mild Steel at Elevated Temperatures", *CORROSION* 2013, paper no. 2348, (Houston, TX, 2013), p. 1-11.
22. J. R. Davis, High-Strength Low-Alloy Steels, Alloying: understanding the basics (No 06117G), 44073.0002, ASM international, Materials Park, OH, 2001, p. 193-202.
23. A. Dugstad, H. Hemmer and M. Seiersten, *Corrosion* **57** (4), 369-378 (2001).
24. L. Onyeji, G. M. Kale and B. M. Kermani, *World Academy of Science, Engineering and Technology, International Journal of Chemical, Molecular, Nuclear, Materials and Metallurgical Engineering* **11** (2), 131-138 (2017).
25. B. Kermani, M. Dougan, J. C. Gonzalez, C. Linne and R. Cochrane, "Development of Low Carbon Cr-Mo Steels With Exceptional Corrosion Resistance for Oilfield Applications", *CORROSION* 2001, paper no. 01065, (Houston, TX, 2001).
26. M. Ueda, H. Takabe and P. I. Nice, "The Development and Implementation of a New Alloyed Steel for Oil and Gas Production Wells", *CORROSION* 2000, paper no. 00154, (Houston, TX, 2000).
27. E. David, C. Robert and G. Rosa, *Journal of Iron and Steel Research (International)* **1** (2011).
28. A. G102-89, (ASTM International West Conshohocken, Pa., 1999).
29. W. S. Tait, *An introduction to electrochemical corrosion testing for practicing engineers and scientists*. (Clair, Racine, Wis., 1994).
30. R. Vera, F. Vinciguerra and M. Bagnara, *Int. J. Electrochem. Sci* **10**, 6187-6198 (2015).
31. G. Ogundele and W. White, *Corrosion* **42** (2), 71-78 (1986).
32. C. Yu, X. Gao and P. Wang, *Electrochemistry* **83** (6), 406-412 (2015).
33. N. Ochoa, C. Vega, N. Pébère, J. Lacaze and J. L. Brito, *Materials Chemistry and Physics* **156**, 198-205 (2015).
34. Y. Ma, Y. Li and F. Wang, *Corrosion Science* **51** (5), 997-1006 (2009).
35. Y. Ma, Y. Li and F. Wang, *Corrosion Science* **52** (5), 1796-1800 (2010).
36. Y. Chen, H. Tzeng, L. Wei, L. Wang, J. Oung and H. Shih, *Corrosion Science* **47** (4), 1001-1021 (2005).
37. H. Luo, C. Dong, K. Xiao and X. Li, *Journal of Materials Engineering and Performance* **26** (5), 2237-2243 (2017).
38. A. H. Seikh, *Hindawi: Journal of Chemistry*, 2013 (Article ID 587514) <http://dx.doi.org/10.1155/2013/587514>, p. 1-7.
39. C. Bian, Z. M. Wang, X. Han, C. Chen and J. Zhang, *Corrosion Science* **96**, 42-51 (2015).
40. Z. Zeng, R. Lillard and H. Cong, *Corrosion* **72** (6), 805-823 (2016).
41. V. Jovic, *Research solutions & Resources* (2003), <http://www.gamry.com> (10/12/2018).
42. G. Brug, A. Van Den Eeden, M. Sluyters-Rehbach and J. Sluyters, *Journal of electroanalytical chemistry and interfacial electrochemistry* **176** (1-2), 275-295 (1984).
43. B. Hirschorn, M. E. Orazem, B. Tribollet, V. Vivier, I. Frateur and M. Musiani, *Electrochimica Acta* **55** (21), 6218-6227 (2010).
44. M. Figueiredo, C. Gomes, R. Costa, A. Martins, C. M. Pereira and F. Silva, *Electrochimica Acta* **54** (9), 2630-2634 (2009).
45. Y. Zhao, S. Yang, C. Shang, X. Wang, W. Liu and X. He, *Materials Science and Engineering: A* **454**, 695-700 (2007).
46. D. A. Lopez, S. Simison and S. De Sanchez, *Electrochimica Acta* **48** (7), 845-854 (2003).
47. A. Dugstad, H. Hemmer and M. Seiersten, *Corrosion*, 2001. **57**(4): p. 369-378.
48. E-112, A., *Standard test methods for determining average grain size*. 2010, ASTM International USA.
49. E.-S. M. Sherif, A. A. Almajid, K. A. Khalil, H. Junaedi and F. H. Latief, *International journal of electrochemical science* **8**, 9360-9370 (2013).
50. C. Palacios and J. Shadley, *Corrosion* **47** (2), 122-127 (1991).
51. D. Matlock, G. Krauss and J. Speer, *Journal of materials processing technology* **117** (3), 324-328 (2001).
52. S. Nešić, *Corrosion Science* **49** (12), 4308-4338 (2007).
53. A. Vuppu and W. Jepson, in *SPE Asia Pacific Oil and Gas Conference*. 1994. Society of Petroleum Engineers.
54. Z. Yin, Y. Feng, W. Zhao, Z. Bai and G. Lin, *Surface and interface analysis* **41** (6), 517-523 (2009).
55. F. Farelas, B. Brown and S. Nestic, "Iron Carbide and its Influence on the Formation of Protective Iron Carbonate in CO₂ Corrosion of Mild Steel", *CORROSION* 2013, paper no. 2291, (Houston, TX, 2013).
56. J. Mora-Mendoza and S. Turgoose, *Corrosion Science* **44** (6), 1223-1246 (2002).
57. K. Ralston and N. Birbilis, *Corrosion* **66** (7), 075005-075005-075013 (2010).
58. Y. Li, F. Wang and G. Liu, *Corrosion* **60** (10), 891-896 (2004).
59. S. Wang, C. Shen, K. Long, H. Yang, F. Wang and Z. Zhang, *The Journal of Physical Chemistry B* **109** (7), 2499-2503 (2005).
60. S. Wang, C. Shen, K. Long, T. Zhang, F. Wang and Z. Zhang, *The Journal of Physical Chemistry B* **110** (1), 377-382 (2006).
61. W. Zeiger, M. Schneider, D. Scharnweber and H. Worch, *Nanostructured Materials* **6** (5-8), 1013-1016 (1995).
62. C. op't Hoog, N. Birbilis and Y. Estrin, *Advanced Engineering Materials* **10** (6), 579-582 (2008).
63. B. Hadzima, M. Janeček, Y. Estrin and H. S. Kim, *Materials Science and Engineering: A* **462** (1-2), 243-247 (2007).
64. S. Wu, Z. Cui, F. He, Z. Bai, S. Zhu and X. Yang, *Materials Letters* **58** (6), 1076-1081 (2004).
65. D. V. Edmonds and R. C. Cochrane, *Materials Research* **8** (4), 377-385 (2005).

FIGURE CAPTIONS

Figure 1. SEM micrographs of as-received samples: (a) Steel A, (b) Steel B and (c) Steel C.

Figure 2. E-logi plots of steel A corroded in 3.5 wt% NaCl solution saturated with 0.5% CO₂ at (A) different pH values and 60°C and (B) different temperatures and unbuffered pH

Figure 3. Corrosion rate (CR) of the steels corroded for 24 hours in 3.5 wt% NaCl solutions saturated with 0.5% CO₂ at 60°C and different pHs:

(a) Steel A; (b) Steel B and (c) Steel C.

Figure 4. Corrosion rate (CR) of the steels corroded for 24 hours in unbuffered 3.5 wt% NaCl solutions saturated with 0.5% CO₂ at different temperatures: (a) Steel A; (b) Steel B and (c) Steel C.

Figure 5. Log-log plots of the 24 hours LPR data for the steels corroded in 3.5 wt% NaCl saturated with 0.5% CO₂ at (A) different pH Values and 60°C and (B) different Temperatures and unbuffered pH.

Figure 6: EIS spectra of steel A corroded in 3.5 wt% NaCl saturated with 0.5% CO₂: at different temperatures and unbuffered pH - (a) Nyquist Plots and (b) Bode plots and at different pHs and 60°C - (c) Nyquist plots and (d) Bode plots.

Figure 7: Simple Randle cell used to fit the EIS data of the specimens after 24 hours linear polarization resistance in 3.5 wt% NaCl solution containing 0.5% CO₂ at different temperatures and pHs.

Figure 8: The fitted EIS plots of steel A corroded in 3.5 wt% NaCl saturated with 0.5% CO₂ at 60°C and unbuffered pH: (a) Nyquist Plots and (b) Bode plots and at pH 3.5 and 60°C (c) Nyquist plots and (d) Bode plots.

Figure 9. SEM micrographs of steel A corroded in 3.5 wt% NaCl solution saturated with 0.5% CO₂ at (a) pH 3.5 and 60°C and (b) at 60°C and unbuffered pH.

Figure 10. SEM micrographs of steel C corroded in 3.5 wt% NaCl solution saturated with 0.5% CO₂ at (a) pH 3.5 and 60°C and (b) at 60°C and unbuffered pH.

Figure 11. XRD Spectra of Steel A corroded in 3.5 wt% NaCl Solution saturated with 0.5% CO₂ at 60°C and pH Conditions

TABLE CAPTIONS

TABLE 1. Elemental specifications of the samples (wt%)

Table 2: ASTM Grain Size number and Ferrite/Pearlite Ratio (%) for the samples

TABLE 3. Tafel extrapolation parameters of the specimens in 3.5 wt% NaCl solution saturated with 0.5% CO₂ at 60°C and different pH values

TABLE 4: Tafel extrapolation parameters of specimens in unbuffered 3.5 wt% NaCl solution saturated with 0.5% CO₂ at different Temperatures

Table 5. EIS fitted data of the specimens in unbuffered 3.5 wt% NaCl saturated with 0.5% CO₂ at different Temperatures

Table 6: EIS fitted data of the specimens in 3.5 wt% NaCl saturated with 0.5% CO₂ at 60°C and different pH

Table 7: EDX Elemental analysis of steel A at two sites of the SEM Micrographs shown in Figure 9

Table 8: EDX Elemental analysis of steel C at two sites of the SEM Micrographs shown in Figure 10

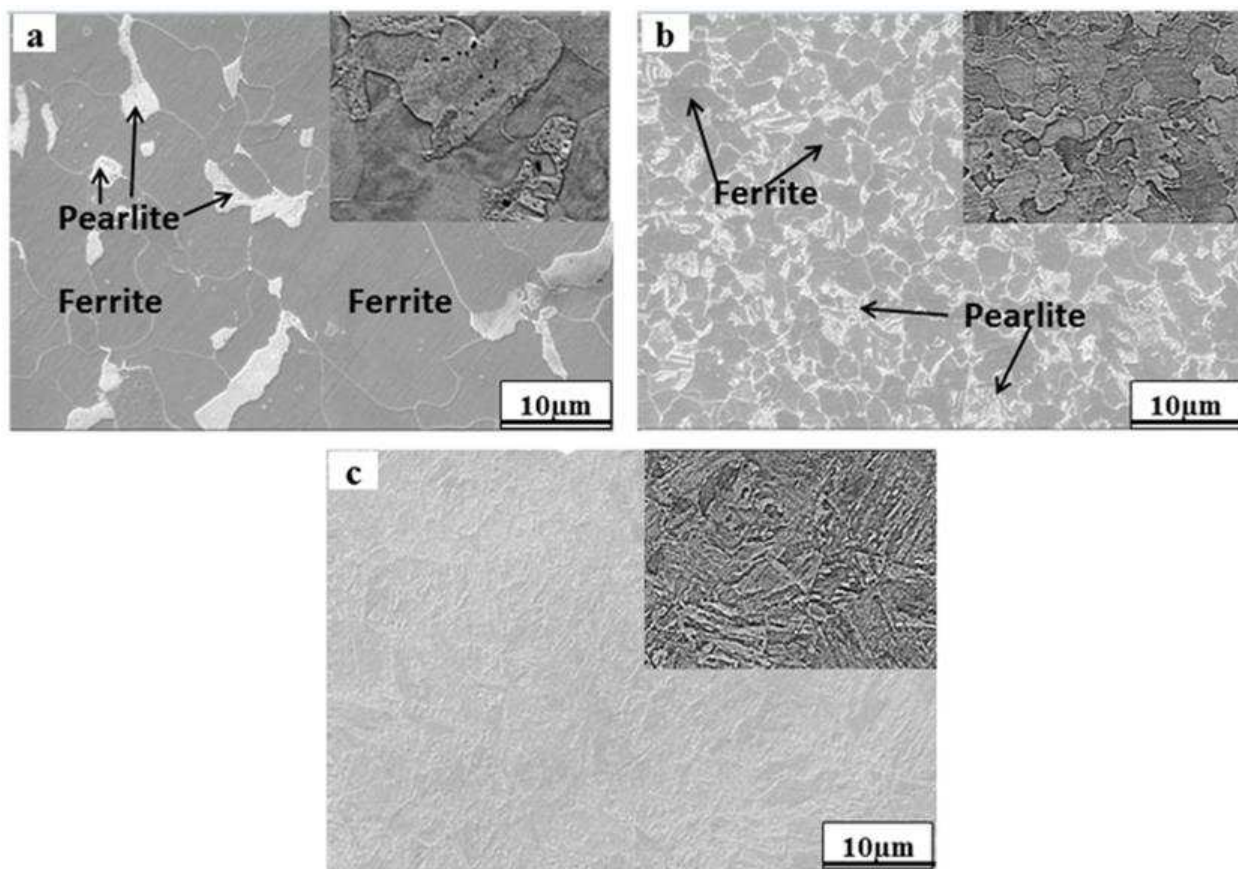


Figure 1. SEM micrographs of as-received samples: (a) Steel A, (b) Steel B and (c) Steel C.

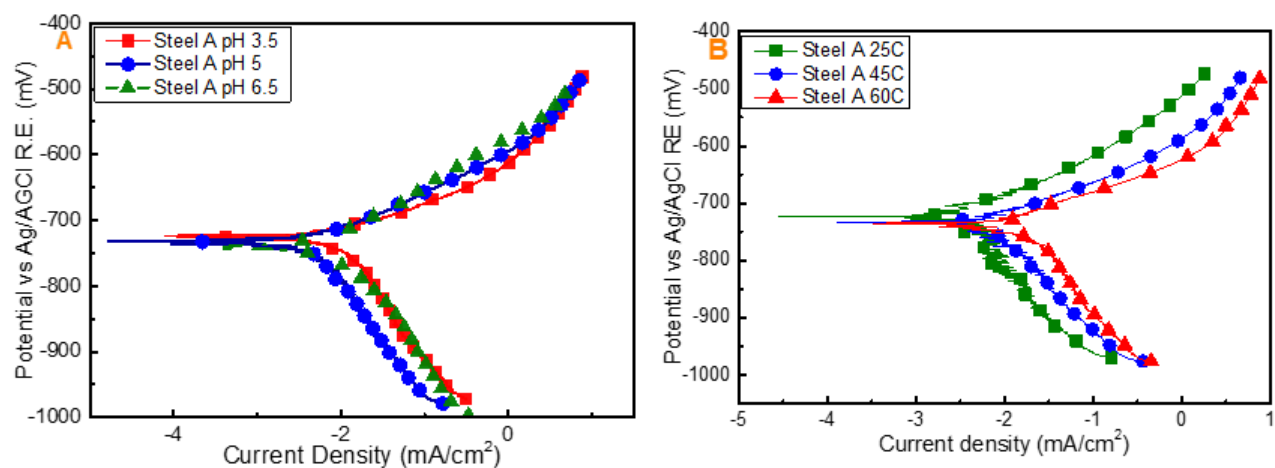


Figure 2. E-logi plots of steel A corroded in 3.5 wt% NaCl solution saturated with 0.5% CO₂ at (A) different pH values and 60°C and (B) different temperatures and unbuffered pH

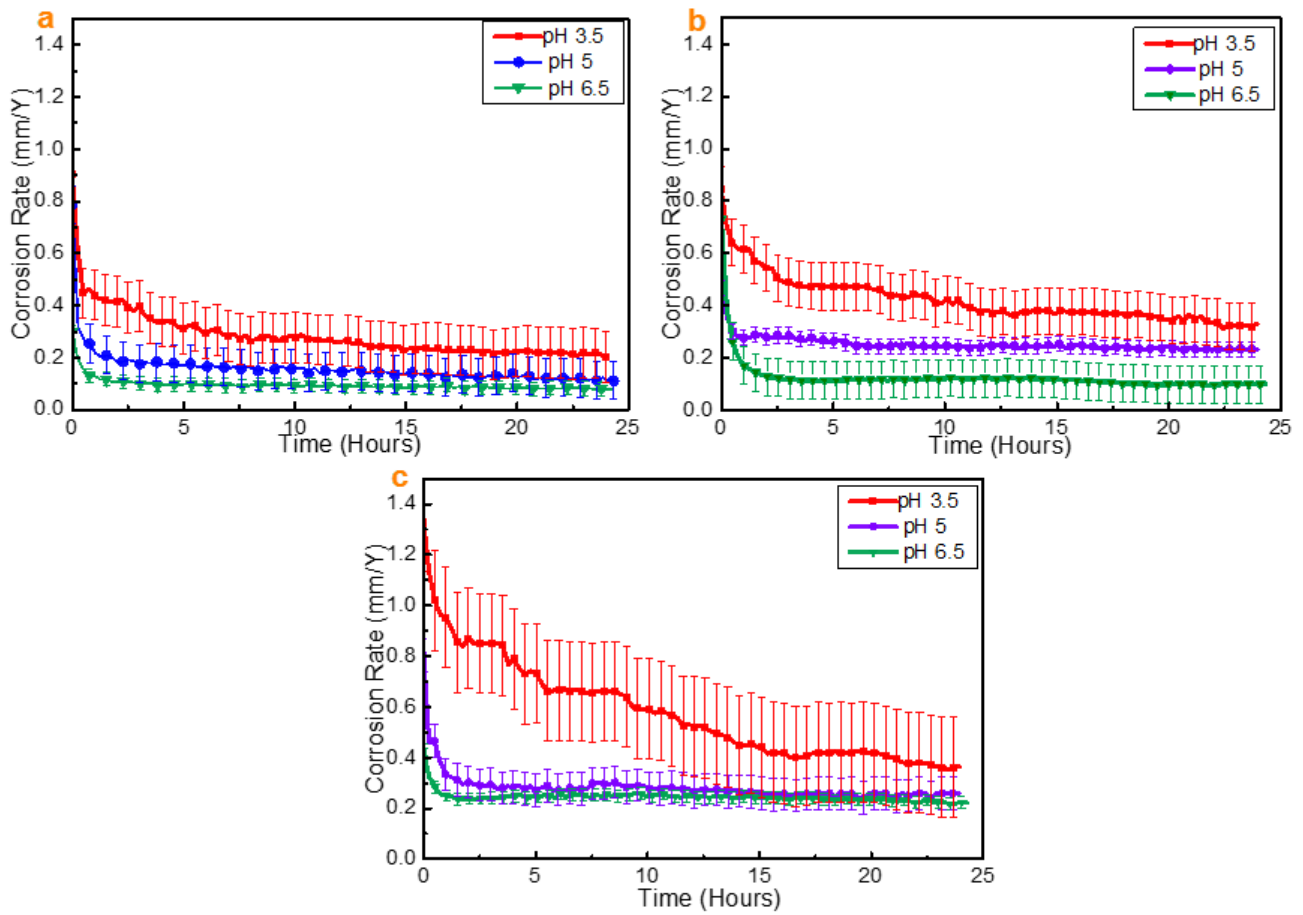


Figure 3. Corrosion rate (CR) of the steels corroded for 24 hours in 3.5 wt% NaCl solutions saturated with 0.5% CO₂ at 60°C and different pHs: (a) Steel A; (b) Steel B and (c) Steel C.

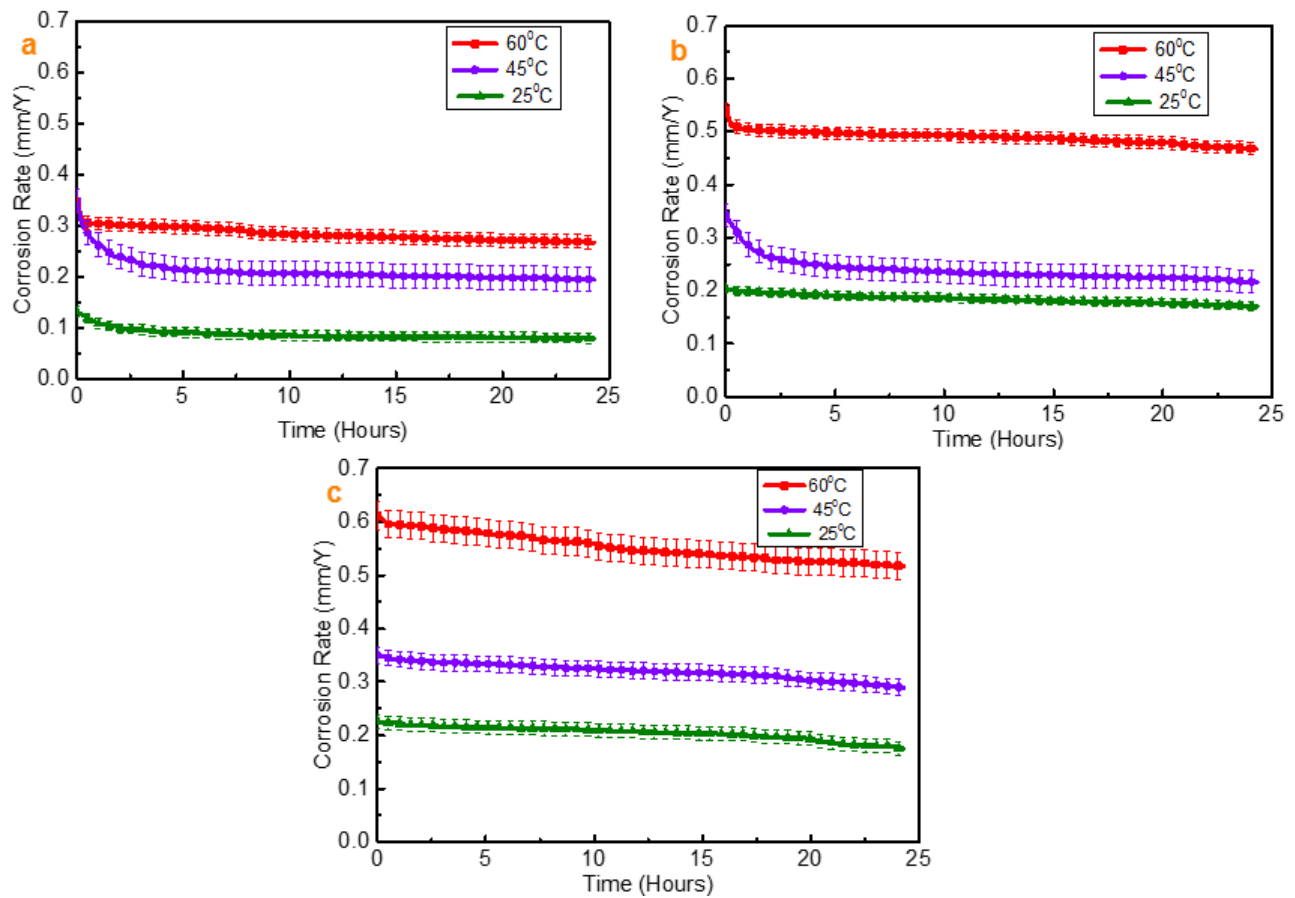


Figure 4. Corrosion rate (CR) of the steels corroded for 24 hours in unbuffered 3.5 wt% NaCl solutions saturated with 0.5% CO₂ at different temperatures: (a) Steel A; (b) Steel B and (c) Steel C.

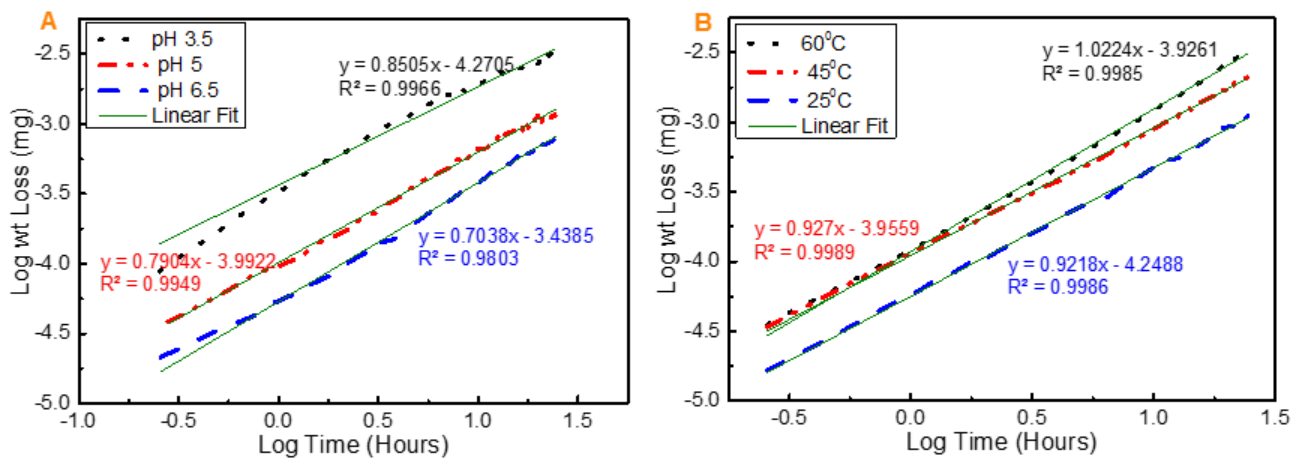


Figure 5. Log-log plots of the 24 hours LPR data for the steels corroded in 3.5 wt% NaCl saturated with 0.5% CO₂ at (A) different pH Values and 60°C and (B) different Temperatures and unbuffered pH.

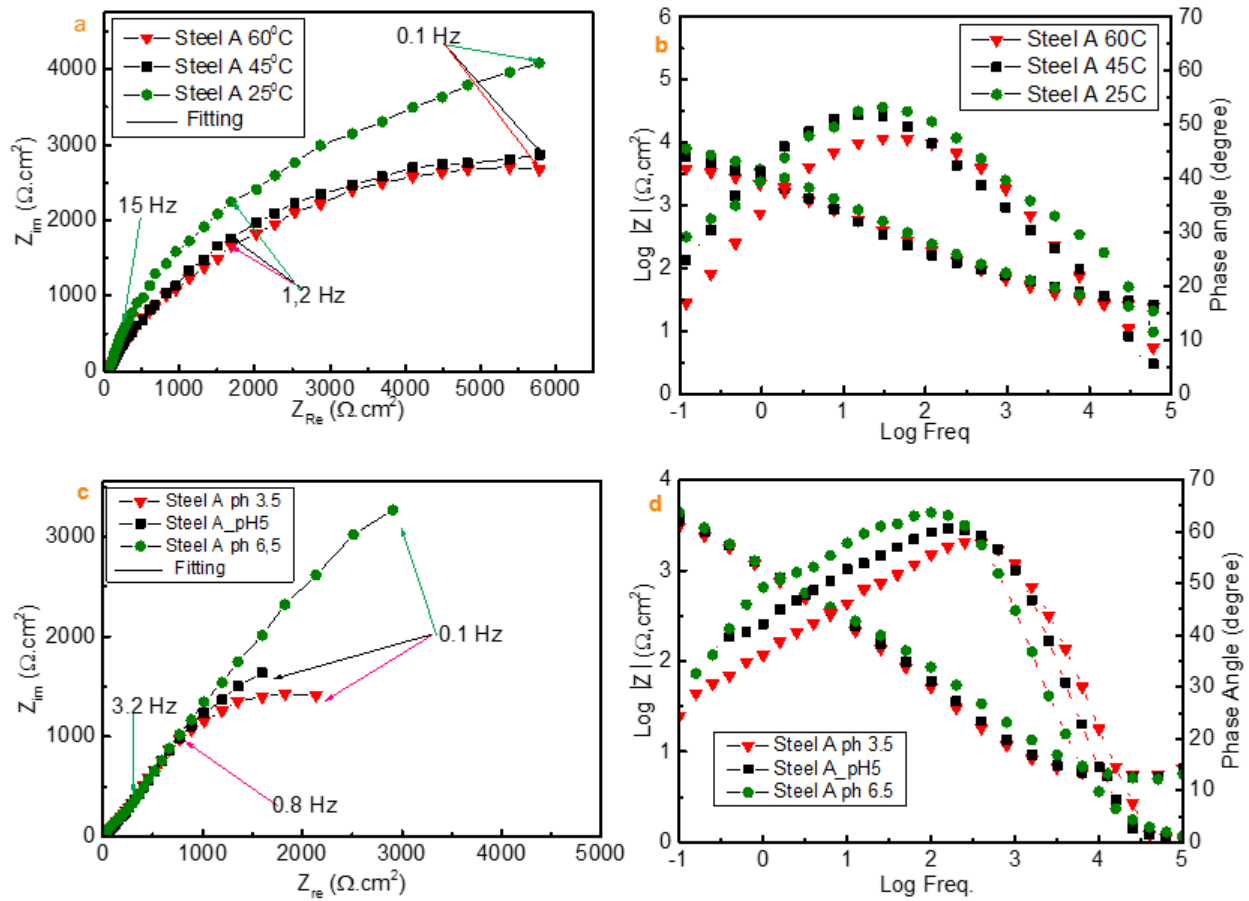


Figure 6: EIS spectra of steel A corroded in 3.5 wt% NaCl saturated with 0.5% CO₂: at different temperatures and unbuffered pH - (a) Nyquist Plots and (b) Bode plots and at different pHs and 60°C - (c) Nyquist plots and (d) Bode plots.

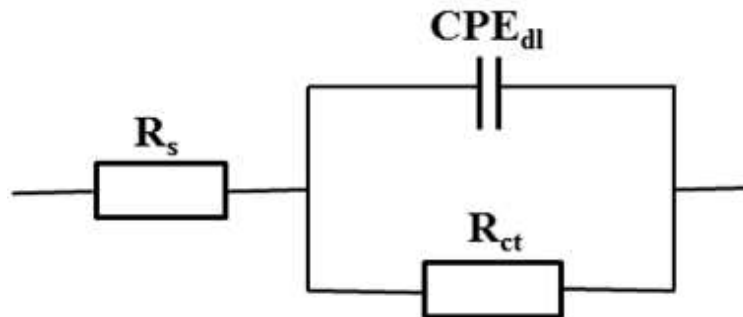


Figure 7: Simple Randle cell used to fit the EIS data of the specimens after 24 hours linear polarization resistance in 3.5 wt% NaCl solution containing 0.5% CO₂ at different temperatures and pHs.

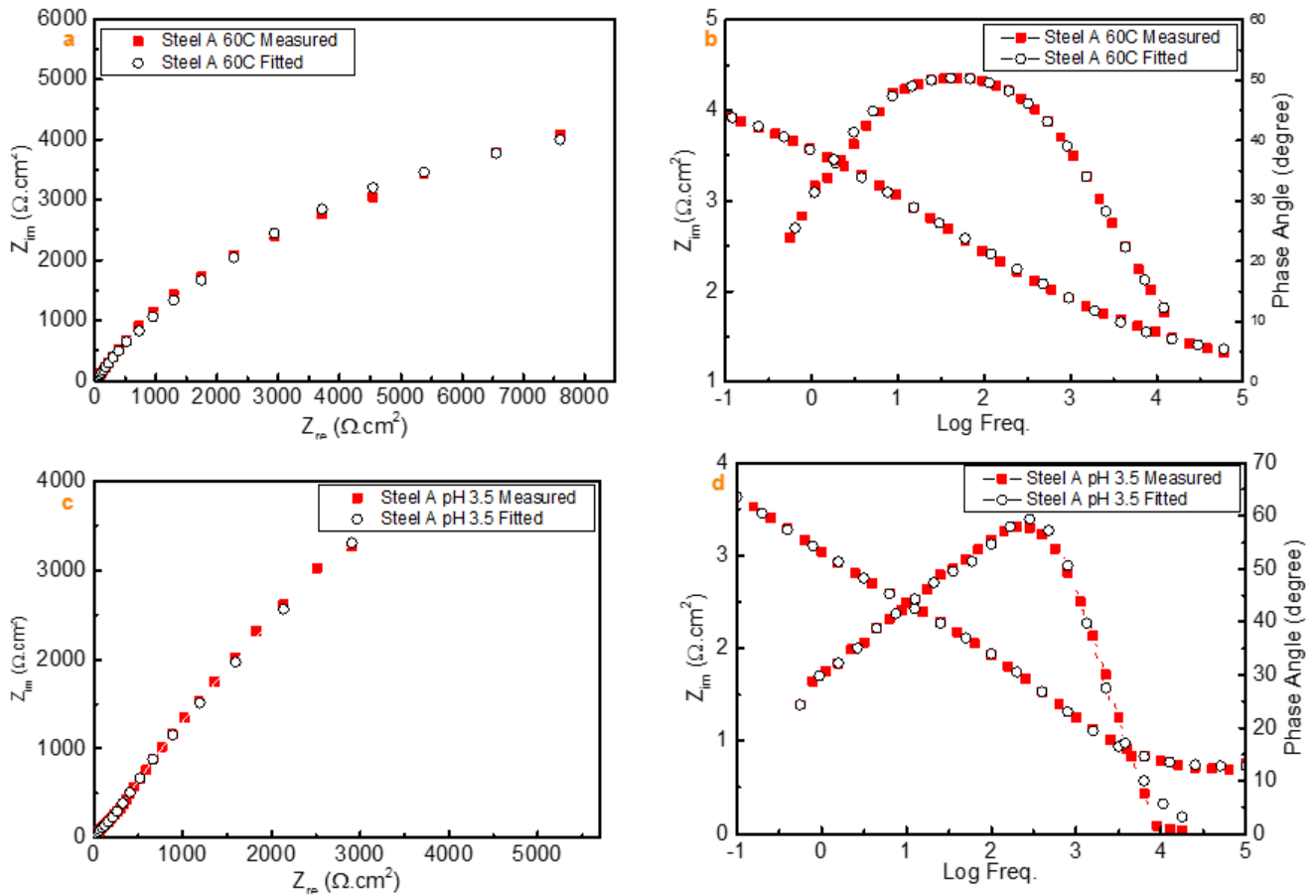


Figure 8: The fitted EIS plots of steel A corroded in 3.5 wt% NaCl saturated with 0.5% CO₂ at 60°C and unbuffered pH: (a) Nyquist Plots and (b) Bode plots and at pH 3.5 and 60°C (c) Nyquist plots and (d) Bode plots.

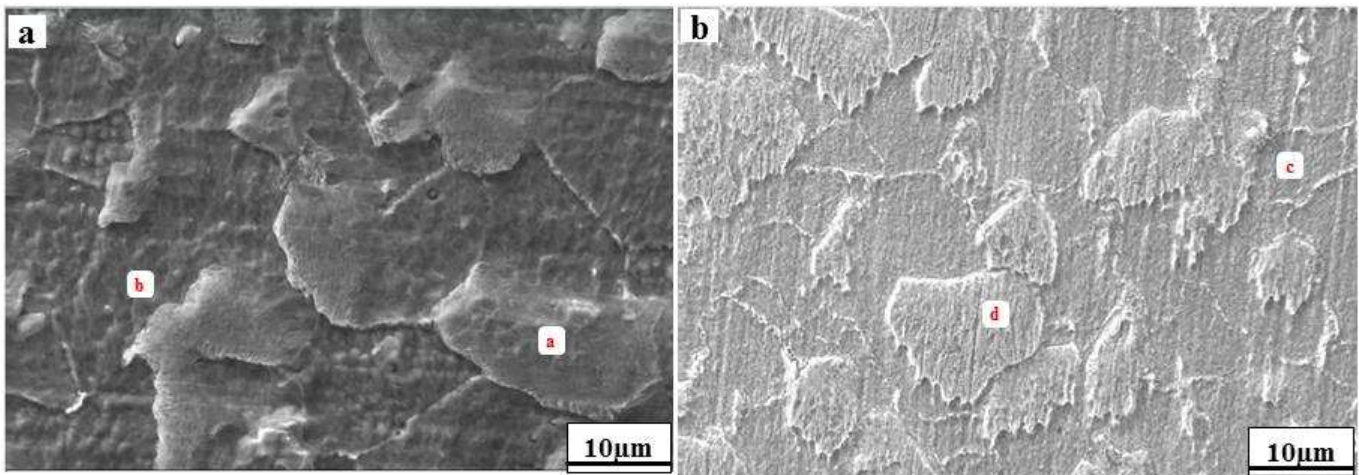


Figure 9. SEM micrographs of steel A corroded in 3.5 wt% NaCl solution saturated with 0.5% CO₂ at (a) pH 3.5 and 60°C and (b) at 60°C and unbuffered pH.

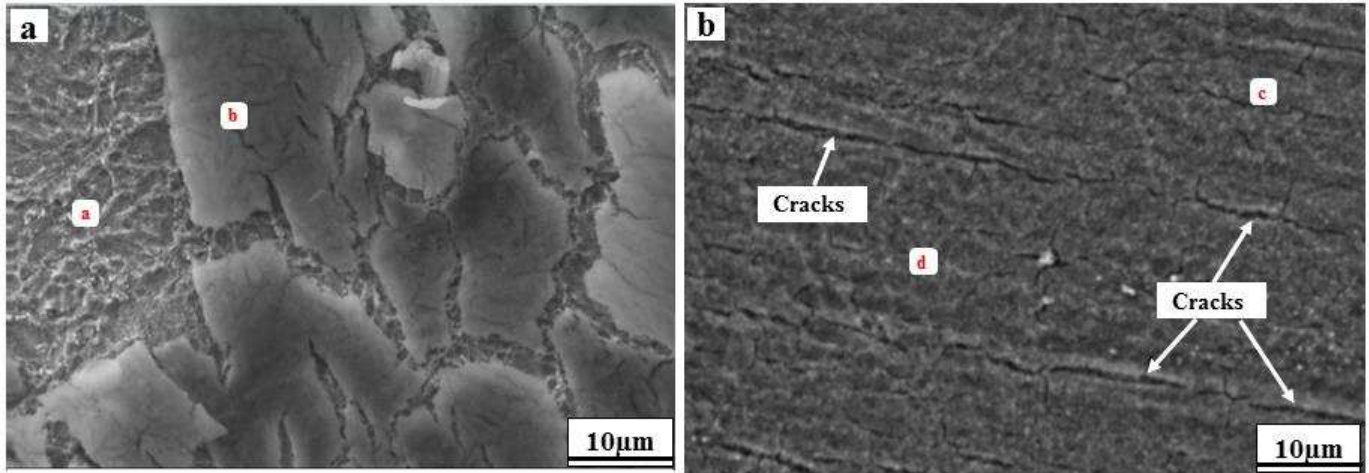


Figure 10. SEM micrographs of steel C corroded in 3.5 wt% NaCl solution saturated with 0.5% CO₂ at (a) pH 3.5 and 60°C and (b) at 60°C and unbuffered pH.

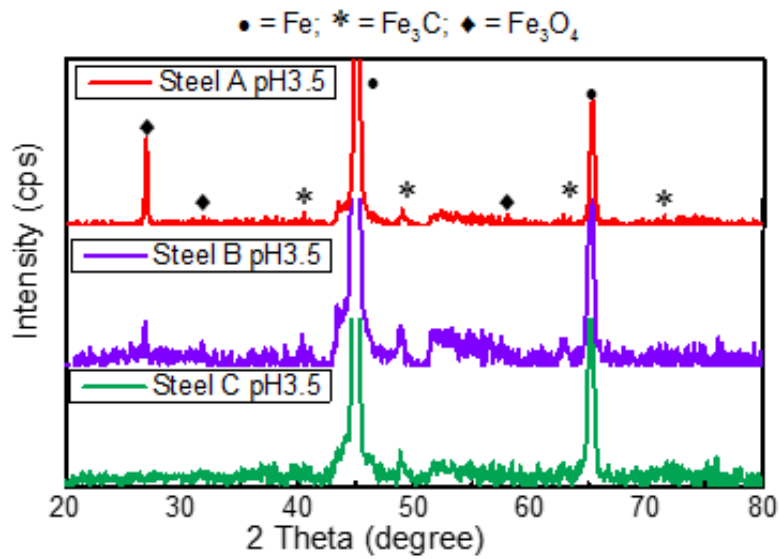


Figure 11. XRD Spectra of Steel A corroded in 3.5 wt% NaCl Solution saturated with 0.5% CO₂ at 60°C and pH Conditions

Table 1: Elemental specifications of the samples (wt%)

Steels	C	Si	Mn	P	S	Cr	Mo	Cu	Fe
A	0.12	0.18	1.27	0.008	0.002	0.11	0.17	0.12	Balance
B	0.22	0.032	1.4	0.012	0.001	0.25	0.07	0.03	Balance
C	0.25	0.26	0.54	0.01	0.001	0.99	0.46	0.098	Balance

Table 2: ASTM Grain Size number and Ferrite/Pearlite Ratio (%) for the samples

Samples	Steel A	Steel B	Steel C
ASTM Grain Size No	3.89	5.57	5.77
Ferrite/Pearlite (%)	63.61	48.23	
Average Grain Size (μm)	68.54	53.4	44.9

Table 3 : Tafel extrapolation parameters of the specimens in 3.5 wt% NaCl solution saturated with 0.5% CO₂ at 60°C and different pH values

Tafel Parameters	pH 3.5			pH 5.0			pH 6.5		
	Steel A	Steel B	Steel C	Steel A	Steel B	Steel C	Steel A	Steel B	Steel C
E _{corr} (mV)	-726	-710	-705	-733	-731	730	-740	-741	-742
β_a (mV/decade)	42	33	43	58	46	55	63	73	54
β_C (mV/decade)	110	112	171	202	134	167	89	96	72
I _{corr} ($\mu\text{Amp}/\text{cm}^2$)	6.70	8.10	8.30	5.30	7.60	7.80	5.10	6.70	7.40
R _p (K Ω)	1.97	1.37	1.80	3.69	1.96	2.30	3.14	2.69	1.81
CR (mm/Y)	0.78	0.94	0.96	0.62	0.88	0.91	0.59	0.78	0.86

Table 4 : Tafel extrapolation parameters of specimens in unbuffered 3.5 wt% NaCl solution saturated with 0.5% CO₂ at different Temperatures

Tafel Parameters	25 ^o C			45 ^o C			60 ^o C		
	Steel A	Steel B	Steel C	Steel A	Steel B	Steel C	Steel A	Steel B	Steel C
E _{corr} (mV)	-723	-720	-710	-735	-720	-760	-735	-733	-722
β _A (mV/decade)	50	52	56	54	53.5	75	58	55	48
β _C (mV/decade)	149	154	170	111	149	105	120	125	135
I _{corr} (μAmp/cm ²)	2.40	3.60	4.10	5.00	8.10	9.00	7.10	8.60	9.60
R _p (KΩ)	6.77	4.69	4.46	3.16	2.11	2.11	2.39	1.93	1.60
CR (mm/Y)	0.28	0.42	0.48	0.58	0.94	1.05	0.82	1.00	1.12

Table 5 EIS fitted data of the specimens in unbuffered 3.5 wt% NaCl saturated with 0.5% CO₂ at different Temperatures

Temp (^o C)	Specimens	R _s		CPE _{dl}		n		R _{ct}		Cdl (μFcm ⁻²)
		Value (Ω.cm ²)	% Error	Value (μF ⁻¹ cm ⁻² Sn ⁻¹)	% Error	Value	% Error	Value (KΩ.cm ²)	% Error	
60	Steel A	29.22	3.45	7.27 * 10 ⁻⁴	3.25	0.60	1.00	5.57	4.27	1.64*10 ⁻⁵
	Steel B	25.9	0.84	5.90 * 10 ⁻⁴	1.10	0.60	0.30	5.41	1.37	1.43*10 ⁻⁵
	Steel C	21.47	1.49	7.10 * 10 ⁻⁴	1.73	0.60	0.41	5.24	2.03	1.97*10 ⁻⁵
45	Steel A	26.53	1.51	6.66 * 10 ⁻⁴	1.60	0.60	0.46	11.5	3.14	1.34*10 ⁻⁵
	Steel B	31.17	2.80	5.10 * 10 ⁻⁴	3.17	0.60	1.00	10.62	6.56	1.29*10 ⁻⁵
	Steel C	26.23	1.23	4.35 * 10 ⁻⁴	1.65	0.60	0.45	5.77	1.85	1.74*10 ⁻⁵
25	Steel A	19.02	2.24	4.60 * 10 ⁻⁴	1.80	0.60	0.59	14.12	3.55	1.06*10 ⁻⁵
	Steel B	28.7	3.25	3.21 * 10 ⁻⁴	3.46	0.60	1.10	12.01	8.6	1.15*10 ⁻⁵
	Steel C	17.4	1.73	1.10 * 10 ⁻⁴	1.56	0.60	0.44	10.84	3.29	1.46*10 ⁻⁵

Table 6 EIS fitted data of the specimens in 3.5 wt% NaCl saturated with 0.5% CO₂ at 60°C and different pH

pH	Specimens	R _s		CPE _{dl}		n		R _{ct}		Cdl (μFcm ⁻²)
		Value (Ω.cm ²)	% Error	Value (μF ⁻¹ cm ⁻² Sn ⁻¹)	% Error	Value	% Error	Value (KΩ.cm ²)	% Error	
6.5	Steel A	5.26	2.4	3.56 * 10 ⁻⁵	9.36	0.90	2.40	56.77	11.23	1.75*10 ⁻⁴
	Steel B	6.63	2.00	2.54 * 10 ⁻⁵	6.90	0.90	2.40	17.66	4.75	1.65*10 ⁻⁵
	Steel C	6.43	2.00	2.13 * 10 ⁻⁶	9.60	0.90	4.20	15.94	9.06	3.63*10 ⁻⁶
5	Steel A	5.49	2.13	1.88 * 10 ⁻⁴	7.40	0.60	4.78	15.43	5.10	1.57*10 ⁻⁶
	Steel B	5.94	2.21	4.0 * 10 ⁻⁵	8.40	0.60	7.40	8.686	3.80	1.08*10 ⁻⁷
	Steel C	5.66	1.95	3.69 * 10 ⁻⁴	3.70	0.60	4.10	8.667	5.20	4.31*10 ⁻⁶
3.5	Steel A	7.85	1.40	4.29 * 10 ⁻⁴	5.60	0.90	2.64	5.973	10.43	2.08*10 ⁻⁴
	Steel B	7.27	1.53	4.84 * 10 ⁻⁵	4.01	0.90	1.89	5.771	4.01	2.36*10 ⁻⁴
	Steel C	5.28	2.20	4.28 * 10 ⁻⁴	6.01	0.90	3.19	4.679	4.40	2.00*10 ⁻⁴

Table 7 : EDS Elemental analysis of steel A at two sites of the SEM Micrographs shown in Figure 9

Element wt%	Site	C	O	Cu	Mn	Cr	Si	Fe
Sample A	a	6.24	4.48	0.74	0.94	0.16	0.26	91.65
pH 3.5	b	8.55	3.43	0.89	0.71	0.26	0.21	85.76
Sample A	c	7.00	2.16	0.80	0.60	0.30	0.20	89.10
60 ⁰ C	d	6.00	2.50	1.00	1.20	0.10	0.20	87.00

Table 8: EDS Elemental analysis of steel C at two sites of the SEM Micrographs shown in Figure 10

Element wt%	Site	C	O	Cu	Mn	Cr	Si	Fe
Sample C	a	2.76	2.79	-	0.59	1.05	0.17	95.44
pH 3.5	b	6.96	4.65	-	0.60	1.49	-	85.39
Sample C	c	11.00	7.00	1.00	1.00	2.00	0.30	77.70
60 ⁰ C	d	13.00	7.00	1.00	1.00	3.00	0.20	74.80